Thermodynamic Sea Ice Growth in the Central Weddell Sea, Observed in Upward-Looking Sonar Data

A. Behrendt[1], W. Dierking[1], and H. Witte[1]

Corresponding author: A. Behrendt, Department of Climate Science, Alfred Wegener Institute, Bussestr. 24, 27570 Bremerhaven, Germany. (Axel.Behrendt@awi.de)

[1]Department of Climate Science, Alfred Wegener Institute, Helmholtz Centre for Polar and Marine Research, Germany.

Abstract. Upward-looking sonar (ULS) data were used to analyse thermodynamic sea ice growth. The study was carried out for an ocean region in the central Weddell Sea, for which data of sea ice thickness variability and of the oceanic heat flux through the ice are rare. In the study area the contribution of sea ice deformation to vertical ice growth is relatively small in some years. This provides the opportunity to simulate thermodynamic sea ice growth considering the influence of a snow cover and of the oceanic heat flux. To this end, a modified version of Stefan's Law was used. The resulting ice thickness variations were then compared with the ULS measurements. For the investigated cases, the best consistency between data and model results was obtained assuming a snow layer of less than 5 cm thickness and average oceanic heat fluxes between 6 and 14 W m^{-2}. It is demonstrated that in conjunction with ice drift data and analytical models for thermal sea ice growth, ULS ice thickness measurements are useful for studying the seasonal cycle of growth and decay, and for inferring the magnitude of the average oceanic heat flux under sea ice.

1. Introduction

Satellite microwave radiometers have been used to monitor Antarctic sea ice since 1979 [*Parkinson and Cavalieri*, 2012]. However, only information about areal parameters, such as ice extent and ice concentration, can be obtained from radiometer data. A complete assessment of sea ice changes and their relevance to global climate requires additional information about the variations of the ice volume [*Lemke et al.*, 2007]; hence, the sea ice thickness must be known [*Wadhams*, 1994]. Due to the lack of submarine data from the Antarctic ocean regions the knowledge about sea ice thickness and its temporal variations is extremely sparse.

To measure sea ice thickness in the Antarctic with sufficient spatial and temporal sampling is still one of the most challenging tasks in sea ice monitoring. Satellite algorithms for the retrieval of sea ice thickness from space-borne radar or laser altimeters are currently under development [e.g., *Giles et al.*, 2008; *Yi et al.*, 2011]. They aim at providing information about circumpolar sea ice thickness on a monthly basis. A first analysis of basin-wide sea ice thickness for the Southern Hemisphere based on laser altimeter data has been published recently by *Kurtz and Markus* [2012]. The error of laser altimetry for ice thickness estimates, however, is still relatively large (on the order of 0.5–0.7 m), mainly because of difficulties in obtaining data of the snow cover thickness on the ice [*Kwok and Cunningham*, 2008].

In this paper, we focus on local studies of temporal ice thickness variations. To date, upward-looking sonars (ULS) are the only instruments for measuring the long term development of sea ice thickness with relatively high accuracy. They are moored at fixed locations and measure the vertical extension of the sub-surface portion of sea ice (the ice "draft"). These data can be converted into total ice thickness assuming hydrostatic equilibrium or by using empirical relations based on data from ice drilling. ULS measurements are not biased toward undeformed ice thickness and are therefore capable of detecting the full range of the sea ice thickness distribution. The accuracy of ice thickness data obtained from ULS measurements is about 5 to 10 cm [*Melling et al.*, 1995]. Most of the ULS studies published so far were carried out in the Arctic. They were mainly concerned with investigating the thickness statistics of different ice classes and pressure ridges [*Melling and Riedel*, 1995; *Melling and Riedel*, 1996; *Fukamachi et al.*, 2006], the long term development of sea ice thickness [*Melling et al.*, 2005], and with ice volume flux studies [*Vinje et al.*, 1998].

In simulations of atmosphere - sea ice - ocean interactions and in global climate simulations thermodynamic sea ice growth is usually modeled by solving equations of heat transfer [*Maykut and Untersteiner*, 1971; M. Losch, personal communication]. This requires special numerical techniques as the thermal properties of sea ice vary with changing temperature and salinity of the ice in a nonlinear way [*Yen*, 1981]. As a simple alternative, thermodynamic ice growth can also be described by analytical methods such as Stefan's Law [*Stefan*, 1891], in which the thermal properties of sea ice are usually taken as constants. At their mooring site, ULS data enable detailed studies of ice thickness variations in the course of a full season. The sea ice thickness distribution is determined by three factors: thermodynamic growth and decay, ice advection toward and away from the measurement site, and convergent and divergent motion of the ice, causing ice thickening due to rafting and ridging and ice thinning due to formation of openings in the ice (e.g. leads) [*Thorndike*, 1975].

In most cases it is not possible to separate the influence of the three before-mentioned terms to the sea ice thickness actually retrieved from ULS data. Hence, it is also difficult to assess the influence of environmental conditions on each of these terms. Most of the studies employing Stefan's Law were carried out in embayments [*Allison*, 1981], fjords [*Høyland*, 2009] or coastal landfast ice [*Purdie et al.*, 2006; *Lei et al.*, 2010], where the ice is less affected by deformation. Our study focuses on thermodynamic ice growth in the central Weddell Sea in single years between 1993 and 2010, in which ice deformation could be neglected. We apply Stefan's Law to estimate the influence of the two limiting factors of thermodynamic ice growth in austral winter: the thermally insulating snow cover on top of the ice and the oceanic heat flux from below. Thermodynamic growth cycles of sea ice have been rarely measured in pack ice. Our ULS measurements therefore provide valuable data to close this gap.

In the next section, we describe the used data and processing methods as well as the measurement sites. Ice advection and the influence of sea ice deformation at our test site are analyzed in section 3. We test the suitability of Stefan's Law for simulating the observed pack ice thickness and discuss its extensions to include effects of a snow cover and the oceanic heat flux in section 4. The results are briefly summarized and discussed in sections 5 and 6.

2. Data and Methods

In the Southern Hemisphere, the largest array of ice-profiling sonars is operated by the Alfred Wegener Institute (AWI). On 13 different locations, a varying number of instruments has been deployed in the Weddell Sea since 1990 [*Behrendt et al.*, 2013]. The ULS data for this study were taken from the PANGAEA archive [*Behrendt et al.*, 2012]. The mooring positions include a transect spanning the Weddell Sea from the tip of the Antarctic Peninsula at Joinville Island in the west to Kapp Norvegia in the east (Fig. 1). A second transect is located on the prime meridian between 59°S and 69.4°S latitude. For the first transect, data series are available since 1990, for the second transect since 1996. Because of logistical reasons, instrument failures and lost moorings, all data series contain significant temporal gaps. An overview of the available data can be found in Figure 2 shown in *Behrendt et al.* [2013] and in an updated version of this figure on the PANGAEA website.

The sea ice in the Weddell Sea is transported in a cyclonic gyre [*Deacon*, 1979], first westward along the continental margin and then northward along the Antarctic Peninsula (Fig. 1). Based on ULS data, the mean monthly ice export was estimated to be 59 $\times$ 10^3 m^3 s^{-1} [*Drinkwater et al.*, 2001]. Our study area is located in the center of the Weddell Gyre at ULS mooring AWI-208 (65°S, 36.5°W, Fig. 1). At AWI-208 the sea ice completely disappears during summer. Further south, a significant fraction of ice remains also in the summer months [*Parkinson and Cavalieri*, 2012]. The first ULS on position AWI-208 was deployed in the period from December 1990 to December 1992. Because of a technical failure no data could be obtained. The second instrument measured between January 1993 and January 1995 with a sampling rate of 4 minutes, and the third one between March 2008 and January 2011 with a sampling rate of 1 minute. The time series of ice draft from this region include the most pronounced thermodynamic cycles of ice growth among all ULS data recorded since 1990 as explained below.

The draft data (d) for this study were converted into total ice thickness (z) (both given in meters) using the empirical relationship

$$z = 0.028 + 1.012\ d. \tag{1}$$

This equation was established from ice drilling in the Weddell Sea. The draft values covered a range between 0.4 and 2.7 m with a coefficient of determination of r^2 of 0.99. The data included cases in which a snow layer was present on the ice. For details see *Harms et al.* [2001], and references cited therein. Due to the constant factor of 2.8 cm in equation (1), thickness values $\leq$0.4 m are overestimated. The bias increases as the ice gets thinner. This, however, is not critical for the analyses presented below.

From their position at depths between 100–150 m, the AWI ULS instruments send short sound pulses at 300 kHz toward the ice-covered ocean surface and measure the travel time of the signal. The processing of the ULS data and the retrieval of ice draft is described in detail in the article by *Behrendt et al.* [2013]. The ice draft is obtained by subtracting the calculated distance between ice bottom and ULS from the instrument depth. Since the properties of the water column between the ULS and the ice are not known, the ice drafts are calculated using a fixed value of sound speed. The results are corrected manually by experienced ice analysts who identify open water leads or thin ice areas in the data series to compensate the error resulting from the assumption of a fixed sound speed. For the accuracy of the data obtained in this way, *Behrendt et al.* [2013] found ±5 cm in the freezing/melting seasons and ±12 cm in winter. The first number compares well with the estimation of *Melling et al.* [1995] given above. When the ice concentration reaches nearly 100 percent in winter, significant biases can occur in the manual ice draft estimation because of the lack of open water leads needed for the correction procedure. Details of the ULS data set from the Weddell Sea, the measurement principle, the data processing and the error estimation can be found in *Behrendt et al.* [2013]. Additional information on ULS measurements is provided in the pioneering studies of *Melling et al.* [1995] and *Melling* [1998].

A bias, which in case of a rough topography of the ice underside results from the finite size of the sonar footprint, can be neglected for undeformed level ice, which is the main focus of this study. A problem is the lack of any information about the local ice drift at the mooring site of the AWI ULS instruments. Hence, we had to look for alternatives. The sea ice drift data used for this study are the Polar Pathfinder Daily Ice Motion Vectors provided by the National Snow and Ice Data Center (NSIDC) [*Fowler et al.*, 2013]. The data are available on a daily basis from October 1978 to December 2012 and are mapped on a 25 km polar stereographic grid. Surface air temperatures at the 2 m level were taken from the ERA Interim reanalysis project of the European Centre for Medium-Range Weather Forecasts (ECMWF). The data we used are provided on a 1.5 deg longitude-latitude grid and include analyses, forecasts, or combinations of both at different time steps.

3. Ice Drift Conditions and Deformation

The local ice thickness is the result of thermodynamic ice growth, of the advection of ice away from or into the area of observation, and of ice deformation. In ULS surveys the measured data reflect the bottom topography of ice fields drifting through the locally fixed sonar footprint. This means that the recorded draft time series may include ice originating from different ice regimes. If the drift speed varies, convergences and divergences may occur which result in the deformation of the ice, creating ridges, rubble fields or open water leads. Such deformation processes disturb the detection of clear thermodynamic growth cycles. Hence, we need to assess for the different ULS positions whether advection of ice from other regimes and local deformation can be neglected relative to the thermodynamic growth. Therefore we analyze ice drift patterns retrieved from satellite data and histograms of ice thickness measured by the ULS instruments.

The fact that pronounced thermodynamic growth cycles seem to occur preferably in the region of AWI-208 can be attributed to the large-scale ice motion in the Weddell Sea, which reveals a relatively low velocity at this and the neighboring position AWI-209 [*Kottmeier and Sellmann*, 1996]. To demonstrate the effect of ice drift on the measured ice draft, we compare the ice seasons 2009–2010 and 2010–2011 at the location of AWI-208.

In the draft records for the position AWI-208 (Fig. 2) every blue dot stands for one corrected measurement of ice draft, converted into total ice thickness. The logging rate of the ULS instrument was one minute, that is, 1440 measurements were recorded per day. The measurements in 2009–2010 (upper graph) are clustered in a band between 0 and 1 m, reflecting the thermodynamic ice growth [*Strass and Fahrbach*, 1998]. The zonal ice drift on the position of AWI-208 in the period 2009–2010 shows initial variations around zero. A short-term peak in the ice thickness is observed in October (A in the figure), at the end of a period of stronger zonal drift toward the east, which most probably transported older deformed ice from the coast of the Antarctic Peninsula into the region. The variation of the northward drift component appears to be slightly smaller. The drift situation of the 1993–1994 season was similar to the ice season 2009–2010, that is, the zonal ice drift varied only slightly around zero. Also in this case, the thermodynamic growth could be recognized relatively clearly in the ULS data record. Similar but less pronounced parts of thermodynamic cycles were measured on ULS positions AWI-209 (east of AWI-208) in 1993 and AWI-229/231 (on the prime meridian) in 1998 [*Behrendt*, 2013]. The mean ice drift in the winter season 2009–2010 (Fig. 3) shows slow northward movement in the region around AWI-208 and higher drift speeds in the boundary regions of the Weddell Gyre. The drift paths indicate that the measured ice started its drift in regions south and southeast of AWI-208. The drift paths from south of AWI-208 seem to be favorable to the detection of thermodynamic growth cycles. The trajectories in 1993–1994 (not shown) were similar to 2009–2010, with even less fluctuations in zonal direction.

The ice in the season 2010–2011 was on average thicker than in the year before. This can be attributed to the stronger ice drift toward the east, which transports thicker ice from the western Weddell Sea toward the center of the gyre. The thickness record for 2010–2011 (Fig. 2, lower graph) shows initial states of thermodynamic growth in April and May. From June onward, the data become more scattered and it is more difficult to identify a single prominent mode in the ice draft distribution. The eastward ice drift dominates at the position of AWI-208. The strong drift event in October/November is reflected in rising ice thickness (marked with B in the Figure). In April/May the northward drift was comparably strong. Throughout the year, the drift in northward direction dominated on timescales of 20 days. The drift situation of 2008–2009 revealed characteristics similar to the 2010–2011 season: pronounced periods of eastward drift and dominating northward drift on timescales of 20 days. The ice draft record in 2008–2009 is also similar to 2010–2011, that is, initial fragments of thermodynamic ice growth were detected in autumn and deformed ice dominated later in the year. The mean ice drift in 2010–2011 (Fig. 3) reveals dominating northward drift in the central Weddell Sea and a strong drift toward the northeast in the northern part of the gyre. The drift paths indicate that the ice measured at AWI-208 early in the year originated from positions south of the mooring. The ice measured by the ULS later in the year started its drift on positions southwest of the mooring. The starting positions in the far south suggest that deformed second-year ice occurred over the ULS position. The ice drifted northward and was later advected by westerly winds across the ULS position. The same pattern of drift trajectories was found for the period 2008–2009 (not shown).

To investigate the ice thickness distribution g(z) at a given ULS location over one season, we follow the approach of *Strass and Fahrbach* [1998] and use the discrete form of the probability density function (PDF). It is estimated by dividing the number of thickness values in an interval between z and z + Δz by the total number of measurements made and additionally by the bin width (here 0.1 m). The distributions plotted in Figure 4 were obtained from the ULS drafts by calculating the ice thickness using the linear relation between draft and thickness quoted above (equation 1). The PDFs show the typical decrease in frequency of larger thickness values. When using exponential functions we found the best fits for ice thickness values between 3 and 16 m. To compare PDFs of different years, we splitted the distributions into ice thickness ranges from 0 to 1.5 m and 1.5 to 16 m. To better distinguish the influences of thermodynamic growth and ice deformation, we calculated the volume fraction (the integral of $z * g(z) * dz$) for the two thickness ranges instead of the area fraction (the integral of $g(z) * dz$ [*Thorndike*, 1975]).

In the four ice seasons shown in Fig. 4, a few drafts of up to 36 m were measured, which we associate with icebergs. The maximum modal ice thickness at about 1 m is more pronounced in seasons with clear thermodynamic growth cycles (1993–1994 and 2009–2010) and is close to the maximum thickness of thermodynamically grown level ice [*Harder and Lemke*, 1994]. Extended ice areas with a mean thickness above about 1 m therefore definitely represent not only thermodynamic growth but also the additional influence of ice deformation. Since ice areas with thicknesses <1 m may also be the result of ongoing thermodynamic ice growth coupled with events of ice deformation, the interpretation of the histogram mode in terms of separating deformed and level ice requires additional information such as the ice drift conditions discussed above.

As an additional criterion, we tested the slope of the exponential function as a qualitative indication of the degree of ice deformation. For the period 2009–2010 we obtained a steep decline which we attribute to the low amount of deformed ice in this season. For the period 1993–1994, however, the slope is similar to the seasons 2008–2009 and 2010–2011, for which the contribution of ice deformation was larger. This may be a result of the lower quality of the fit, caused by the larger scatter of the values above 10 m (Fig. 4). A more robust criterion is the difference of the relative volume fractions in the ice thickness ranges 0–1.5 m and 1.5–16 m. It is smaller for the periods 2009-2010 and 1993-1994 (indicating less deformation) and larger for periods 2008–2009 and 2010–2011. In 2010–2011, e. g., there is about 16% more ice volume above 1.5 m than in the season before (Fig. 4).

4. Simulation of Sea Ice Growth

4.1. Stefan's Law for Snow-Covered Ice

Stefan's description of thermodynamic sea ice growth [*Stefan*, 1891] is based on the assumption that the heat loss during the freezing process is directed upward and is completely balanced by the latent heat of fusion of the ice [*Allison*, 1981]. We use Stefan's Law without considering solar shortwave radiative fluxes, which is justified since we focus only on conditions in austral winter. The growth rate dH/dt is thus exclusively determined by the energy balance at the ice/water interface [*Petrich and Eicken*, 2010]

$$\rho_i L_i \frac{dH}{dt} = F_c - F_w, \tag{2}$$

where ρ_i is the bulk density, L_i is the latent heat of freezing of sea ice, F_c is the upward conductive heat flux through the ice and F_w is the oceanic heat flux from below. The term on the left hand side of the equation represents the latent heat flux due to freezing (F_L).

In the first step of our analysis, we neglect the oceanic heat flux and only consider the presence of snow on the ice. In case of a snow layer of thickness h on top of an ice layer of thickness H, the conductive heat flux on the right hand side of equation (2) can be expressed by Fourier's Law of heat conduction for two layers

$$\rho_i L_i \frac{dH}{dt} = \frac{T_w - T_0}{\frac{H}{\lambda_i} + \frac{h}{\lambda_s}}, \tag{3}$$

where T_w is the water temperature, T_0 is the snow surface temperature, and λ_i and λ_s are the thermal conductivities of ice and snow, respectively. To solve this equation analytically one usually assumes that the snow thickness increases linearly with ice thickness: $h = rH$. The validity of this assumption is discussed below. The analytic solution of equation (3) then is

$$H = \sqrt{\frac{2\lambda_i}{\rho_i L_i (1 + \frac{\lambda_i}{\lambda_s} r)} \int_0^T (T_w - T_0) dt}. \tag{4}$$

For the absence of snow ($r = 0$) the equation reduces to the classic solution of *Stefan* [1891]. Since the snow surface temperature T_0 is usually not known, another possibility is to use the air temperature. The net heat flux between the atmosphere and the snow surface (F_a) can then be parameterized by the linear approximation $F_a = k(T_0 - T_a)$ [*Leppäranta*, 1993]. The atmospheric surface temperature (T_a) is taken from measurements at automatic weather stations close to the site of the ULS mooring or from daily temperature provided by meteorological data centers such as ECMWF. The effective heat transfer coefficient k is a function of wind speed, snow insulation, radiation, humidity, evaporation, and atmospheric stability which can be determined from measurements of sea ice growth under different meteorological conditions [*Anderson*, 1961; *Petrich and Eicken*, 2010; Eicken, personal communication]. Since the coefficient k includes turbulent heat fluxes as well as net longwave radiative fluxes [*Petrich and Eicken*, 2010], one can assume $F_a = F_c$ [*Leppäranta*, 1993] and equation (3) can then be expressed as

$$\rho_i L_i \frac{dH}{dt} = \frac{T_w - T_a}{\frac{1}{k} + \frac{H}{\lambda_i} + \frac{h}{\lambda_s}}. \tag{5}$$

The analytic solution, using h = rH is

$$H = \sqrt{\frac{2\lambda_i}{\rho_i L_i \left(1 + \frac{\lambda_i}{\lambda_s} r\right)} \int_0^T (T_w - T_a)dt + A^2} - A, \quad with\ A = \left(\frac{\lambda_i}{k(1 + \frac{\lambda_i}{\lambda_s} r)}\right). \tag{6}$$

This equation is the basis for our estimations of the influence of snow on the observed ice thickness. In the following we provide the values we used for the different constants in equation 6, supplemented by additional information and a sensitivity analysis.

The density of sea ice was set to $\rho_i = 0.92$ g cm^{-3}, which is a typical value for first-year level ice with no air inclusions. *Timco and Frederking* [1996] found values between 0.90

and 0.94 g cm^{-3} for sea ice below the water surface. Varying ρ_i between 0.90 and 0.94 has only a negligible effect on the calculated ice thickness, which is below the accuracy of ULS measurements in winter. Following *Pringle et al.* [2007], we use a value of $\lambda_i = 2.2$ W m^{-1} K^{-1} for the thermal conductivity of sea ice. *Leppäranta* [1993] and *Petrich and Eicken* [2010] suggest $\lambda_s = 0.1\lambda_i$ for snow. *Lei et al.* [2010] used temperature measurements together with a thermodynamic snow/sea ice model and obtained a value of $\lambda_s = 0.2$ W m^{-1} K^{-1}, which did not reveal any significant seasonal variations. This value is consistent with results of *Sturm et al.* [2002] for new snow in the Arctic. However, the value of λ_s depends strongly on the snow type. In the Antarctic the values range between 0.07 W m^{-1} K^{-1} for new snow and 0.45 W m^{-1} K^{-1} for very hard wind slab [*Sturm et al.*, 1998]. As we expect more young snow on first-year level ice in the Weddell Sea [*Massom et al.*, 2001], we varied λ_s between 0.13 and 0.19 W m^{-1} K^{-1}. Using this range of values, the variations in the calculated ice thickness hardly exceeded the ULS accuracy. For the heat transfer coefficient, one can apply the relationship λ_i/k = 0.1 m [*Leppäranta*,1993], which means that k = 22 W m^{-2} K^{-1}. *Petrich and Eicken* [2010] assumed values between 10 and 45 W m^{-2} K^{-1} based on measurements of sea ice growth under different environmental conditions (see also *Anderson* [1961]). To determine the best value for k, we varied this parameter in our simulations (see section 4.3). The smallest deviations between the model and our observations were obtained for k $\geq$ 60 W m^{-2} K^{-1}. As noted by *Petrich and Eicken* [2010], a value of k = 45 W m^{-2} K^{-1} is valid for a snow layer of 13 cm on ice of 1 m thickness. Since we obtain smaller snow depths in the presence of an oceanic heat flux, we consider k = 60 W m^{-2} K^{-1} as a realistic value for our simulations (note that only corresponding results are discussed in section 4.3). The effect of increasing the k value above 60 W m^{-2} K^{-1} was found to be negligible for the simulated ice growth. We took L_i = 334 J g^{-1}, which lies between the values of 333 J g^{-1} reported by *Fukusako* [1990] and 335 J g^{-1} from *Leppäranta* [1993]. A variation of ±1 J g^{-1} can be ignored in ice thickness calculations.

The water temperature was set to the freezing point T_w = -1.8°C and the daily mean surface air temperature on the grid point closest to AWI-208 was taken from ECMWF reanalysis (ERA-Interim). According to the station measurements of **Bracegirdle and Marshall** [2012, Fig. 2], the bias in annual mean and winter surface air temperatures of the ERA-Interim data is ≤1°C in the northern part of the Antarctic Peninsula. We therefore expect that the bias on our ULS position is approximately of same magnitude. This bias shifts the calculated ice thickness by a maximum of only 6 cm at the end of the growth season. The effect on the calculated ice thickness is therefore considered small enough to be neglected for most of the growth period.

To take into account the fact that some ice detected in the ULS-data at the beginning of freeze-onset may have grown at another location and was advected over the ULS position, we shifted the starting day for the calculated ice thickness backwards by two weeks. After an initial ice growth of a few centimeters in early April 1993 and March 2009, the ice growth weakened considerably due to the increasing air temperatures in the following weeks. The effect on the maximum ice thickness in winter is comparably low (few centimeters) and can therefore be neglected.

4.2. Simulation of Ice Growth in the Presence of Snow

Since we assume h=rH (with h as snow thickness and H as ice thickness) for including the effect of a snow cover on thermodynamic sea ice growth, we need to assess to what extent this relationship is valid. In the Weddell Sea, the correlation coefficient R between the thickness of sea ice and the snow layer lies in the range 0.43–0.67 [*Massom et al.*, 1997]. For new level ice, carrying only the recent snow accumulation, the correlations were found to be higher (R = 0.8). In regions with highly deformed multi-year ice, such as close to the Antarctic Peninsula, the correlation decreases to R = 0.39. In the central Weddell Sea, close to position AWI-208, only first-year ice exists. The standard deviations of both the measured snow depth and level ice thickness in the central Weddell Sea are very low ($\pm$0.02 m) [*Massom et al.*, 1997]. Therefore we assume that the relation h = rH is a reasonable model for our calculations of thermodynamic ice growth.

Because of lower precipitation rates compared to the Bellinghausen, Amundsen and Ross Sea sectors, snow depths in the central Weddell Sea are low [*Massom et al.*, 2001]. They typically vary from 5 to 10 cm, and the mean values in different regions rarely exceed 30 cm [*Massom et al.*, 2001]. High values of snow depth (50–100 cm) are measured mainly on multiyear ice along the Peninsula in the western Weddell Sea [*Lange and Eicken*, 1991; *Massom et al.*, 1997].

When a winter snow cover becomes thick enough, its weight depresses the snow/ice interface below the water line. The slush formed from the flooded snow layer may freeze and consolidate, resulting in the formation of snow (meteoric) ice. In this way meteoric ice can contribute a significant amount to the total sea ice thickness. Although in the Antarctic flooding of sea ice is a widespread phenomenon [*Massom et al.*, 2001], ice core analyses suggest that snow-ice formation makes only a moderate contribution to the total sea ice mass in the Weddell Sea. To obtain the snow thickness at which flooding occurs we follow the approach of *Massom et al.* [1997]. Assuming undeformed sea ice floating on seawater and isostatic balance, the ratio of snow to ice thickness (r_{flood}) at which flooding starts, is

$$r_{flood} \geq \frac{(\rho_w - \rho_i)}{\rho_s} = 0.34 \tag{7}$$

Here we used an ice density $\rho_i = 0.92$ g cm^{-3}, a water density of $\rho_w = 1.03$ g cm^{-3} and a snow density of $\rho_s = 0.32$ g cm^{-3} (based on *Massom et al.* [2001]). If, for example, a snow layer becomes thicker than 17 cm, level ice of 0.5m thickness is flooded. Since flooding is less common in the central Weddell Sea and snow layers on first-year level ice are typically thin, we do not consider the case of flooding.

After the initial test with variable heat transfer coefficient k (see above), our first simulations include two unknown variables: the parameter r, describing the coupling between snow and ice layer thickness, and the thermal conductivity of snow (λ_s). The parameter r was varied between 0 (i.e., no snow) and 0.34 (threshold for flooding), and the snow conductivity between 0.13 and 0.19 W m^{-1} K^{-1}. Using these values together with daily mean surface air temperatures and the constants described in the previous section, the theoretical ice growth was calculated from equation (6). We then varied the parameters r and λ_s stepwise to obtain all possible realistic combinations. Note that for the calculation of each curve showing the increase of ice thickness as a function of time, the values of r and λ_s were assumed to be constant over the full growth period.

For comparisons between the ice growth simulations and the ULS observations, we used the statistical mode of the observed ice thickness distributions as representative for the level ice thickness as explained above. On a daily basis, the mode shows very strong fluctuations, which is also evident in the scattering of the single ULS measurements (Fig. 2, upper part). We therefore calculated weekly distributions to obtain the statistical mode (Figs. 5 and 6). The mode values were interpolated linearly to match the daily scale of the calculated ice thickness. All results from equation (6) were compared to the mode of the observations. Those simulations that revealed the smallest root mean square (RMS) deviation from the observations were then used to derive the possible ranges of r and λ_s and thus to determine the growth rate and thermal conductivity of the snow cover.

The weekly mode for the season 1993–1994 in Figure 5a shows fluctuations, especially in the first half of the record. The two bumps around week 6 and week 12 clearly deviate from the square-root law of thermodynamic ice growth. The histograms of the weekly thickness distributions occasionally reveal a broadening around the mode, which complicates the detection of a clear signal. We assume that our estimation of the mode has an average error of approximately ± 5 cm (reflected by our choice of the histogram bin size, see Figs. 5 and 6), which lies within the accuracy of single ULS measurements. For bi-modal distributions recognized in the second half of the record the second mode had to be selected, as the first mode occurs in the thickness class 0–5 cm, indicating refreezing leads (Figs. 5 and 6). In September/October (Fig. 5a, weeks 24–27) the histograms cover a wide range of ice thickness values. This indicates highly variable ice conditions over the ULS position for which a characterization by the modal ice thickness is too simplistic. The apparent jump in ice thickness between weeks 26 and 27 may be a result of changing ice drift patterns. In this period the zonal ice drift turned to a more westerly direction, while a strong positive northward drift anomaly occured at the same time (not shown). These changes may have created convergences and divergences in the ice pack.

The ice formation starts in April when the air temperatures drop below the freezing point of seawater (Fig. 5b, note that we apply the model only for the time of growing ice thickness). At the beginning of the ice season the thickness values are scattered in the upper meter of the water column. *Strass and Fahrbach* [1998] showed that the end of this initial period roughly corresponds to the closing of the ice cover, i.e., the time when the ice concentration rises rapidly to nearly 100 percent. From July onward, the thermodynamic ice growth is easier to identify. With the beginning of October, the clustered values show a scatter of approximately ±10 cm, which can be caused by e.g. the ULS measurement uncertainty in the case of closed ice covers with no leads. A more detailed discussion of the scattered values is provided in section 5.

The ice growth in 1993–1994 extended over approximately 180 days (Fig. 5). The ice started growing with 2.5 cm d^{-1} in late April and continued with growth rates of $\leq$1 cm d^{-1} until the end of June. From June on, the rate decreased to less than 0.5 cm d^{-1}. When neglecting the snow cover the thermodynamic ice growth is overestimated by a factor of almost two when applying equation (6). Once a thin snow cover is included, the observed ice thickness can be well described by the model. The model results also reveal the dependence of sea ice thickness on air temperature. The values of possible snow thicknesses (Fig. 5b) were derived from those simulation results that showed the minimum RMS deviation (in this case 0.14 m) relative to the observations. They cover the range from a thin snow cover of 14 cm thickness and low thermal conductivity (r = 0.15, λ_s = 0.13 W m^{-1} K^{-1}) to a thicker snow cover of 26 cm and higher thermal conductivity (r = 0.29, λ_s = 0.19 W m^{-1} K^{-1}). A variation of the statistical mode of the ice thickness by ±5 cm increases the span of snow thickness in November from 14–26 cm to 12–31 cm. Since, as mentioned above, the observed snow thickness rarely exceeds a value of 10 cm in the central Weddell Sea, a thin snow cover and lower thermal conductivity are more likely.

As in 1993–1994, the ice growth in 2009–2010 extended over approximately 180 days. The ice growth rates varied from 3 cm d^{-1} in early April to $\leq$1 cm d^{-1} until mid July. Then, the ice growth decreased down to $\leq$0.5 cm d^{-1}. The modal ice thickness fluctuated less than in 1993–1994 (Fig. 6). Except for the first month, the mode closely follows the growth of the level ice (Fig. 6b). The ice grew faster than in 1993–1994 as the growth period was not interrupted by rising air temperatures, such as in July/August 1993. In 2009–2010 the ice reached its thickness maximum at around 1 m already in August/September, which is about one month earlier than in 1993–1994 (note that the ice season also started about three weeks earlier). The record of 2009–2010 also shows scattering of the data in the upper meter of the water column in the initial phase of ice growth. As the ice in 2009–2010 was thicker compared to 1993–1994, the growth simulations yielded slightly lower snow thicknesses. The results with the minimum RMS deviation (0.11 m) from the observations suggest a range for the snow thickness between 10 and 19 cm (with values of r = 0.09, $\lambda_s = 0.13$ W m^{-1} K^{-1} and r = 0.18, $\lambda_s = 0.19$ W m^{-1} K^{-1}). A variation of the statistical mode of the ice thickness by ± 5 cm increases the span of the snow thicknesses in November from 10–19 cm to 9–20 cm.

4.3. Consideration of the Oceanic Heat Flux

The ocean always contains a reservoir of heat, which maintains a heat flux through the ice toward the colder atmosphere [*Petrich and Eicken*, 2010]. Besides the snow cover on the ice, this additional heat flux limits the ice growth. The oceanic heat flux is typically highly variable. It mainly depends on the temperature in the oceanic mixed layer [*McPhee*, 1992; *Lei et al.*, 2010], the roughness of the ice bottom [*Holland et al.*, 1997] and on the ice motion and the current velocities under the ice [*McPhee*, 1992]. It is also affected by the ice growth itself and the associated thermohaline convection under the ice [*Allison*, 1981], and by changes in ice concentration and solar radiation absorbed by the seawater.

To include the oceanic heat flux in our calculations we used Stefan's Law (equation 6) extended by a term describing the cumulative effect of oceanic heat [*Allison*, 1981; *Lei et al.*, 2010]

$$H = \sqrt{\frac{2\lambda_i}{\rho_i L_i \left(1 + \frac{\lambda_i}{\lambda_s} r\right)} \int_0^T (T_w - T_a) dt + A^2} - A - \frac{1}{\rho_i L_i} \int_0^T F_w \, dt, \tag{8}$$

where F_w is the oceanic heat flux, and the factor A is equal to the definition for equation (6) above.

Because we lack independent measurements of the oceanic heat flux, we use equation (8) to estimate the necessary average flux F_w for the considered period by comparing the simulations to our ULS measurements. To estimate all possible combinations of r , λ_s and F_w, we again changed these parameters stepwise in a systematic manner and extracted those combinations that showed the smallest RMS deviation relative to the ULS measurements. For r and λ_s we used the ranges of values given above, the oceanic heat flux was varied between 0 and 20 W m^{-2}. Results are shown in Table 1. We again considered an error of ±5 cm in the modal ice thickness.

The fitting curves for the season 1993–1994 showed a minimum RMS deviation from the observed ice thickness mode of 0.13 m and thus yielded a small improvement compared with the simulations neglecting F_w (previous section). The ranges of the parameters include situations without snow and a high oceanic heat flux of 17 W m^{-2} and a 14 cm thick snow layer with an oceanic heat flux of 3 W m^{-2}. The large span of possible values can be attributed to the strong fluctuations of the ice thickness mode. As discussed earlier, scenarios with snow thickness below 10 cm are more realistic in the Weddell Sea. This would slightly narrow down the possible range for the oceanic heat flux to 4–17 W m^{-2}. The scenarios showing the smallest RMS deviation included the full range of values for

λ_s (0.13–0.19 W m^{-1} K^{-1}).

The example shown in Figure 7a is an extreme scenario without snow and a very high oceanic heat flux of 17Wm^{-2}. The calculated ice thickness fits relatively well to the observed ice growth until September but deviates from the observed mode in October and November. The second scenario (Fig. 7b) includes a snow cover increasing in thickness up to 10 cm over the ice growth season and a moderate oceanic heat flux of 5Wm^{-2}. In this case the fit becomes better at the end of the growth season, but still seems to underestimate the ice thickness mode from October onward. Both scenarios are equivalent, that is, they reveal the same RMS deviation from the observed mode (0.13 m).

For the years 2009–2010 (Fig. 8) only few combinations of the parameters r and F_w showed the smallest RMS deviation of 0.08 m from the detected thickness mode. The corresponding deviation of the snow-only model was 0.11 m, which suggests that the inclusion of the oceanic heat flux slightly increased the quality of the fits. For the nominal mode, the best fit is obtained for a very thin snow layer of only 1 to 2 cm thickness but for relatively high oceanic heat fluxes between 10 and 12 W m^{-2} (Table 1). Increasing the mode by 5 cm yields a higher number of possible snow thickness-heat flux combinations. They include snow thicknesses between 0 and 4 cm and oceanic heat fluxes between 6 and 14 W m^{-2}. When decreasing the mode by 5 cm the snow thickness varies between 3 and 5 cm, and the span of possible oceanic heat fluxes lies between 8 and 10 W m^{-2}. Since the ice thickness mode observed in 2009–2010 better follows the square-root law of thermodynamic ice growth, the estimated ranges for the parameters r and F_w are significantly smaller than in 1993–1994. As in 1993–1994, the scenarios showing the smallest RMS deviation included the full range of values for λ_s (0.13–0.19 W m^{-1} K^{-1}).

The fit in Figure 8a shows that the observed ice growth can be reasonably well described by equation (8), assuming a high oceanic heat flux of 12 W m^{-2} and a very thin snow depth increasing up to 1 cm. The curve in figure 8b is equivalent with 8a (RMS = 8 cm), but yields a slightly better agreement with the observations at the end of the growth season.

In our model simulations we assumed that F_w in equation (8) is constant over the entire ice growth period. Under real conditions the oceanic heat flux usually starts at higher values and decreases with time, and is furthermore subject to strong intra-seasonal fluctuations [*Allison*, 1981; *Lytle and Ackley*, 1996; *Lei et al.*, 2010].

5. Discussion

In the central Weddell Sea, the average length of the sea ice growth period amounts to approximately 180 days. Low-frequency variations of air temperatures are clearly reflected in the ice thickness changes. The theoretical maximum thickness of level ice of about 1 m [*Harder and Lemke*, 1994] is in line with our ULS observations. Most observations in the Antarctic are in the range between 0.5 and 0.7 m [*Petrich and Eicken*, 2010]. In the western Weddell Sea, *Worby et al.* [2008, Table 3] found a mean thickness of 0.91±0.75 m for the level ice (which we interpret as mean of the ice thickness mode) from 810 ship-based observations. Those findings compare well with our observations.

Since we had no direct measurements of snow thickness and oceanic heat flux, we varied their magnitudes in a systematic manner when carrying out the simulations, and used the RMS deviation between theoretical results and observations as a criterion for the quality of the fits. The best agreement between simulations and observations for the period 1993–1994 were obtained when snow layers of 0–14 cm, oceanic heat fluxes between 3 and 17 W m^{-2} and a snow heat conductivity between 0.13 and 0.19 W m^{-1} K^{-1} were assumed. Since observed snow depths in the central Weddell Sea hardly exceed 10 cm, a smaller range of the oceanic heat flux is more likely. In the ULS data from 2009–2010 the ice growth cycle could be more clearly identified. The best fits were found for snow depths between 1 and 2 cm and oceanic heat fluxes ranging from 10 to 12 W m^{-2}.

The snow depths and heat fluxes that we obtained in our simulations are within realistic boundaries. For the oceanic heat flux under Antarctic landfast ice *Lei et al.* [2010] found monthly mean values varying between 14 W m^{-2} in December and 3 W m^{-2} in September, with an average of 4.2 $\pm$ 2.4 W m^{-2} for the period May–September 2006. *Allison* [1981] calculated ocean-to-ice heat fluxes, which varied between 0 and about 40 W m^{-2} near Mawson, Antarctica. They used a mean heat flux of 9 W m^{-2} to explain the observed growth of snow-free landfast ice by applying Stefan's Law. *Lytle and Ackley* [1996] reported mean values of 6–8 $\pm$ 2 W m^{-2} in the period February–June 1992 for sea ice at different sites in the western Weddell Sea. The position of AWI-208 lies about 20 degrees further east, and we obtained higher upper bounds (14 and 17 W m^{-2}) in our flux estimations.

In our analysis, the determination of oceanic heat fluxes and snow depths relies critically on the detection of a clear thermodynamic growth signal in the ice thickness histograms. In our data, we found clear deviations from the assumption of a one-dimensional wintertime ice growth. All shown ULS records (Figs. 5 and 6) include strong signals scattered in the upper meter of the water column at the beginning of each ice season (mainly in April and May). The signals observed in April represent most probably reflections from frazil crystals that are mixed in the upper water layer by Langmuir circulation during the early stages of ice formation. Also air bubbles as a result of breaking waves in leads may have caused the observed reflections from below the water surface [*Drucker et al.*, 2003]. The statistical mode of the reflection depths during these periods lies above the growth curve from Stefan's Law, which compares with our assumption that it results from air bubbles and/or frazil ice crystals in the water column. These problems are well known in the processing of ULS data, and the retrieved ice thicknesses from the initial ice growth have to be critically examined. Also some values in May/June that range from 0.5 to 1 m are too large to be explained by thermodynamic growth of level ice. Possibly these signals originate from pancake ice, which is herded and compacted by wind action. Such aggregates can reach mean thicknesses of 40–70 cm [*Lange et al.*, 1989]. Figure 8a suggests that the detection of a thermodynamic growth signal is possible after the first 2 weeks of ice formation.

In general ice draft fluctuations can result from (1) changes in the ice drift direction, (2) variations of surface air temperature, (3) snowfall/snowmelt events causing a deviation from the assumption h=rH, (4) fluctuations in the oceanic heat flux, (5) occasional flooding events and (6) measurement and/or processing uncertainty. Taking these factors and the ULS uncertainty into account, it is not possible to derive daily oceanic heat flux variations from the balance $F_w = F_c - F_L$ (Eq. 2). Therefore we used the average heat flux in our simulations. In field studies, temporal variations of the oceanic heat flux are mostly derived using the so-called residual method [*Lytle and Ackley*, 1996; *Høyland*, 2009; *Lei et al.*, 2010]. This method is based on Eq. 2 and requires ice-temperature profiles and high-accuracy measurements of ice accretion/ablation from the ice underside. This can be achieved by using thermistor strings in combination with drill hole measurements [e.g., *Lei et al.*, 2010] or by deploying special ice mass balance buoys [*Lei et al.*, 2014].

6. Conclusions

We used ice thickness data measured by means of ULS to study thermodynamic sea ice growth in the central Weddell Sea. Two seasons with dominating thermodynamic growth cycles could be identified (1993–1994 and 2009–2010). In these years, the ice drift conditions were found to be favorable for a clear detection of such cycles, because the advection of thicker deformed ice from further west was relatively low over the ULS position. This was confirmed by calculating ice drift trajectories that crossed the ULS position. The ice in 1993–1994 and 2009–2010 originated from regions south of the mooring position. The drift patterns indicate a certain degree of ice deformation due to convergence and divergence, but the thermodynamic growth cycles in the northward drifting floes are nevertheless clearly identifiable. In 2008–2009 and 2010–2011 the drift trajectories indicate that the detected ice originated from a larger area southwest of the mooring position, which is usually covered by deformed second-year ice.

We applied modified versions of Stefan's Law to simulate thermodynamic ice growth and to estimate the snow cover on the ice and the oceanic heat flux from below. We found that Stefan's Law is very well suited to simulate thermodynamic ice growth by comparing the theoretical results with the modal ice thickness derived from the ULS data. This study also confirms the importance of including snow thickness and the upward ocean heat flux in the analyses of sea ice thickness variations. Our results compare well with previous measurements of snow thickness and oceanic heat fluxes in the Weddell Sea. It furthermore offers detailed observations of sea ice growth and melt cycles in a region, in which measurements of sea ice thickness are still very sparse. Our observations therefore provide important information which can be directly used to validate the ice thickness obtained from simulations with sea ice models or from satellite altimetry. For example, by comparing model results with ULS observations, *Timmermann et al.* [2009] demonstrated that their FESOM sea ice model still underestimates the ice thickness in the central Weddell Sea.

As demonstrated in our study, the heat flux integrated over large parts of the ice growth season can in principle be obtained using a modified version of Stefan's Law (Eq. 8), if thermodynamic ice growth is dominant, and the effect of ice deformation can be neglected. This requires that the unknowns in the equation (in particular ice and snow thickness, but also the thermal conductivity of snow and the heat transfer to the atmosphere) must be known with high accuracy. If this is the case, e.g. along longer profiles or over certain regions, it will offer a chance to interpolate or supplement the point measurements of the oceanic heat flux over larger areas.

Acknowledgments. We thank two anonymous reviewers for their constructive comments. The ULS data used in this study are available at http://doi.pangaea.de/10.1594 /PANGAEA.785565. The ice-drift data were obtained from NSIDC (http://nsidc.org/data /docs/daac/nsidc0116_icemotion.gd.html), and the surface air temperature data from ECMWF (ERA-Interim) (http://apps.ecmwf.int/datasets/data/interim_full_daily). This study was supported by the projects FA 436/3-1 and FA 436/3-2 in the framework of the priority programme SPP 1158 of the Deutsche Forschungsgemeinschaft (DFG). We dedicate this work to the memory of Eberhard Fahrbach, who always followed our ULS studies with large interest and helpful advice.

References

Allison, I. (1981), Antarctic ice growth and oceanic heat flux, *IAHS Publ.*, *131*, *56*(193), 119–139.

Anderson, D. L. (1961), Growth rate of sea ice. *J. Glaciol.*, *3*, 1,170–1,172.

Behrendt, A., W. Dierking, E. Fahrbach, and H. Witte (2012), Sea ice draft measured by upward looking sonars in the Weddell Sea (Antarctica), *PANGAEA data library*, doi:10.1594/PANGAEA.785565.

Behrendt, A., W. Dierking, E. Fahrbach, and H. Witte (2013), Sea ice draft in the Weddell Sea, measured by upward looking sonars, *Earth Syst. Sci. Data*, *5*, 209–226, doi:10.5194/essd-5-209-2013.

Behrendt, A. (2013), The Sea Ice Thickness in the Atlantic Sector of the Southern Ocean, Ph.D. Thesis, Dep. of Physics and Electrical Engineering, University of Bremen, Bremen, Germany (available at http://hdl.handle.net/10013/epic.41879).

Bracegirdle, T. J., and G. J. Marshall (2012), The Reliability of Antarctic Tropospheric Pressure and Temperature in the Latest Global Reanalyses, *J. Climate*, *25*, 7138–7146.

Deacon, G. E. R. (1979), The Weddell gyre, *Deep-Sea Res.*, *26A*, 981–995.

Drinkwater, M., X. Liu, and S. Harms (2001), Combined satellite- and ULS-derived sea-ice flux in the Weddell Sea, *Ann. Glaciol.*, *33*, 125–132.

Drucker, R., S. Martin, and R. Moritz (2003), Observations of ice thickness and frazil ice in the St. Lawrence Island polynya from satellite imagery, upward looking sonar, and salinity/temperature moorings, *J. Geophys. Res.*, *108(C5)*, doi:10.1029/2001JC001213.

Fowler, C., W. Emery, and M. Tschudi (2013), Polar Pathfinder Daily 25 km EASE-Grid Sea Ice Motion Vectors, Versions 1 and 2, mean gridded fields, *National Snow and Ice Data Center (NSIDC)*, Boulder, Colorado USA.

Fukamachi, Y., G. Mizuta, K. I. Ohshima, T. Toyota, N. Kimura, and M. Wakatsuchi (2006), Sea ice thickness in the southwestern Sea of Okhotsk revealed by a moored ice-profiling sonar, *J. Geophys. Res.*, *111*, C09018, doi:10.1029/2005JC003327.

Fukusako, S. (1990), Thermophysical Properties of Ice, Snow, and Sea Ice, *Int. J. Thermophys.*, *11(2)*, 353–372.

Giles, K. A., S. W. Laxon, and A. P. Worby (2008), Antarctic sea ice elevation from satellite radar altimetry, *Geophys. Res. Lett.*, *35*, L03503, doi:10.1029/2007GL031572.

Harder, M., and P. Lemke (1994), Modeling the extent of sea ice ridging in the Weddell Sea, in *The polar oceans and their role in shaping the global environment, Geophysical Monograph 85*, *The Nansen Centennial Volume*, edited by O. M. Johannessen, R. D. Muench, and J. E. Overland, pp. 187–197, AGU, Washington D.C., USA.

Harms, S., E. Fahrbach, and V. H. Strass (2001), Sea ice transports in the Weddell Sea, *J. Geophys. Res.*, *106*, 9,057–9,073.

Holland, M. M., J. A. Curry, and J. L. Schramm (1997), Modeling the thermodynamics of a sea ice thickness distribution, 2. Sea ice/ocean interactions, *J. Geophys. Res.*, *102(C10)*, 23,093–23,107.

Høyland, K. V. (2009), Ice thickness, growth and salinity in Van Mijenfjorden, Svalbard, Norway, *Polar Res.*, *28*, 339–352, doi:10.1111/j.1751-8369.2009.00133.x.

Kottmeier, C., and L. Sellmann (1996), Atmospheric and oceanic forcing of Weddell Sea ice motion, *J. Geophys. Res.*, *101*, 20,809–20,824.

Kurtz, N. T., and T. Markus (2012), Satellite observations of Antarctic sea ice thickness and volume, *J. Geophys. Res.*, *117*, C08025, doi:10.1029/2012JC008141.

Kwok, R., and G. F. Cunningham (2008), ICESat over Arctic sea ice: Estimation of snow depth and ice thickness, *J. Geophys. Res.*, *113*, C08010, doi:10.1029/2008JC004753.

Lange, M. A., S. F. Ackley, P. Wadhams, G. S. Dieckmann, and H. Eicken (1989), Development of Sea Ice in the Weddell Sea, *Ann. Glaciol.*, *12*, 92–96.

Lange, M. A., and H. Eicken (1991), The Sea Ice Thickness Distribution in the Northwestern Weddell Sea, *J. Geophys. Res.*, *96(C3)*, 4,821–4,837.

Lei, R., Z. Li, B. Cheng, Z. Zhang, and P. Heil (2010), Annual cycle of landfast sea ice in Prydz Bay, east Antarctica, *J. Geophys. Res.*, *115*, C02006, doi:10.1029/2008JC005223.

Lei, R., N. Li, P. Heil, B. Cheng, Z. Zhang, and B. Sun (2014), Multiyear sea ice thermal regimes and oceanic heat flux derived from an ice mass balance buoy in the Arctic Ocean, *J. Geophys. Res.*, *119*, doi:10.1002/2012JC008731.

Lemke, P., J. Ren, R. B. Alley, I. Allison, J. Carrasco, G. Flato, Y. Fujii, G. Kaser, P. Mote, R. H. Thomas, and T. Zhang (2007), Observations: Changes in Snow, Ice and Frozen Ground, in *Climate Change 2007: The Physical Science Basis. Contribution of Working Group I to the Fourth Assessment Report of the Intergovernmental Panel on Climate Change*, edited by S. Solomon, D. Qin, M. Manning, Z. Chen, M. Marquis, K. B. Averyt, M. Tignor, and H. L. Miller, pp. 337–384, Cambridge University Press, Cambridge, United Kingdom and New York, NY, USA.

Leppäranta, M. (1993), A Review of Analytical Models of Sea-Ice Growth, *Atmos. Ocean*, *31(1)*, 123–138.

Lytle, V. I., and S. F. Ackley (1996), Heat flux through sea ice in the western Weddell Sea: Convective and conductive transfer processes, *J. Geophys. Res.*, *101(C4)*, 8,853–8,868.

Massom, R., M. R. Drinkwater, and C. Haas (1997), Winter snow cover on sea ice in the Weddell Sea, *J. Geophys. Res.*, *102(C1)*, 1,101–1,117.

Massom, R., H. Eicken, C. Haas, M. O. Jeffries, M. R. Drinkwater, M. Sturm, A. P. Worby, X. Wu, V. I. Lytle, S. Ushio, K. Morris, P. A. Reid, S. G. Warren, and I. Allison (2001), Snow on Antarctic Sea Ice, *Rev. Geophys.*, *39(3)*, 413–445.

Maykut, G. A., and N. Untersteiner (1971) Some Results from a Time-Dependent Thermodynamic Model of Sea Ice, *J. Geophys. Res.*, *76*, 1,550–1,575.

McPhee, M. G. (1992), Turbulent Heat Flux in the Upper Ocean Under Sea Ice, *J. Geophys. Res.*, *97(C4)*, 5,365–5,379.

Melling, H., P. H. Johnston, and D. A. Riedel (1995), Measurements of the Topography of Sea Ice by Moored Subsea Sonar, *J. Atmos. Ocean. Tech.*, *12*, 589–602.

Melling, H., and D. A. Riedel (1995), The underside topography of sea ice over the continental shelf of the Beaufort Sea in the winter of 1990, *J. Geophys. Res.*, *100*, 13,641–13,653.

Melling, H., and D. A. Riedel (1996), Development of seasonal pack ice in the Beaufort Sea during the winter of 1991-1992: A view from below, *J. Geophys. Res.*, *101*, 11,975–11,991.

Melling, H. (1998), Sound Scattering from Sea Ice: Aspects Relevant to Ice-Draft Profiling by Sonar, *J. Atmos. Ocean. Tech.*, *15*, 1,023–1,034.

Melling, H., D. A. Riedel, and Z. Gedalof (2005) Trends in the draft and extent of seasonal pack ice, Canadian Beaufort Sea, *Geophys. Res. Lett.*, *32*, L24501, doi:10.1029/2005GL024483.

Parkinson, C. L., and D. J. Cavalieri (2012), Antarctic sea ice variability and trends, 1979-2010, *The Cryosphere*, *6*, 871–880, doi:10.5194/tc-6-871-2012.

Petrich, C., and H. Eicken (2010), Growth, Structure and Properties of Sea Ice, in *Sea Ice (second edition)*, edited by D. N. Thomas, and G. S. Dieckmann, pp. 23–77, Blackwell Publishing Ltd.

Pfirman, S. L., R. Colony, D. Nürnberg, H. Eicken, and I. Rigor (1997), Reconstructing the origin and trajectory of drifting Arctic sea ice, *J. Geophys. Res.*, *102*, C6, 12,575–12,586.

Pringle, D. J. , H. Eicken, H. J. Trodahl, and L. G. E. Backstrom (2007), Thermal conductivity of landfast Antarctic and Arctic sea ice, *J. Geophys. Res.*, *112*, C04017, doi:10.1029/2006JC003641.

Purdie, C. R., P. J. Langhorne, G. H. Leonard, and T. G. Haskell (2006), Growth of first-year landfast Antarctic sea ice determined from winter temperature measurements, *Ann. Glaciol.*, *44*, 170–176.

Stefan, J. (1891), Über die Theorie der Eisbildung, insbesondere über die Eisbildung im Polarmeere, *Ann. Phys.*, *42*, 269–286.

Strass, V. H., and E. Fahrbach (1998), Temporal and Regional Variation of Sea Ice Draft and Coverage in the Weddell Sea Obtained from Upward Looking Sonars, in *Antarctic*

Sea Ice: Physical Processes, Interactions and Variability, *Antarct. Res. Ser.*, *74*, edited by M. O. Jeffries, pp. 123–139, AGU, Washington, D.C.

Sturm, M., K. Morris, and R. Massom (1998), The winter snow cover of the West Antarctic pack ice: Its spatial and temporal variability, in *Antarctic Sea Ice: Physical Processes Interactions and Variability*, *Antarct. Res. Ser.*, *74*, edited by M. O. Jeffries, pp. 19–40, AGU, Washington, D.C.

Sturm, M., D. K. Perovich, and J. Holmgren (2002), Thermal conductivity and heat transfer through the snow on the ice of the Beaufort Sea, *J. Geophys. Res.*, *107(C21)*, 8043, doi:10.1029/2000JC000409.

Thorndike, A. S., D. A. Rothrock, G. A. Maykut, and R. Colony (1975), The Thickness Distribution of Sea Ice, *J. Geophys. Res.*, *80*, 4,501–4,513.

Timco, G. W., and R. M. W. Frederking (1996), A review of sea ice density, *Cold. Reg. Sci. Technol.*, *24*, 1–6.

Timmermann, R., S. Danilov, J. Schröter, C. Böning, D. Sidorenko, and K. Rollenhagen (2009), Ocean circulation and sea ice distribution in a finite element global sea ice-ocean model, *Ocean Model.*, *27*, doi:10.1016/j.ocemod.2008.10.009.

Vinje, T., N. Nordlund, and A. Kvambekk (1998), Monitoring ice thickness in Fram Strait, *J. Geophys. Res.*, *103*, 10,437–10,449.

Wadhams, P. (1994), Sea ice thickness changes and their relation to climate, in *The polar oceans and their role in shaping the global environment, Geophysical Monograph 85*, *The Nansen Centennial Volume*, edited by O. M. Johannessen, R. D. Muench, and J. E. Overland, pp. 337–361, AGU, Washington D.C., USA.

Worby, A. P., C. A. Geiger, M. J. Paget, M. L. Van Woert, S. F. Ackley, and T. L. DeLiberty (2008), Thickness distribution of Antarctic sea ice, *J. Geophys. Res.*, *113*, C05S92, doi:10.1029/2007JC004254.

Yen, Y. C. (1981), Review of thermal properties of snow, ice and sea ice, *CRREL Rep. 81–10*, pp. 1–27, Cold Reg. Res. and Eng. Lab., Hanover, N. H.

Yi, D., H. J. Zwally, and J. W. Robbins (2011), ICESat observations of seasonal and interannual variations of sea-ice freeboard and estimated thickness in the Weddell Sea, Antarctica (2003-2009), *Ann. Glaciol.*, *52(57)*, 43–51.

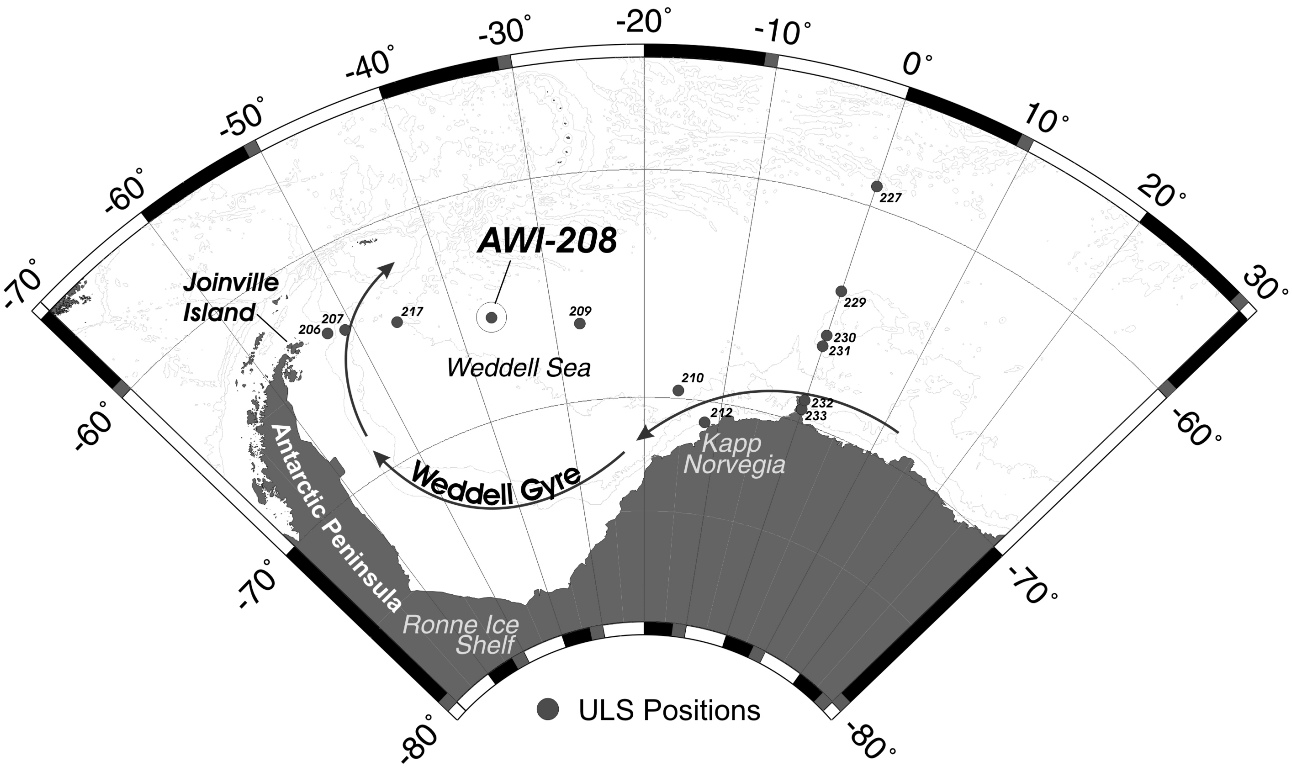

Figure 1. The study area in the Weddell Sea. Black dots with numbers represent the positions of the ULS-mooring array.

Table 1. Estimated Ranges for Snow Parameters and Oceanic Heat Flux (Equation 8)[a]

Years	Scenario	r	Snow Depth [cm]	F_w [W m^{-2}]	RMS Dev. [cm]
1993–1994	mode	0–0.15	0–14	3–17	13
	mode +5 cm	0–0.09	0–8	5–16	14
	mode -5 cm	0.02–0.19	2–17	3–14	12
2009–2010	mode	0.01–0.02	1–2	10–12	8
	mode +5 cm	0–0.04	0–4	6–14	10
	mode -5 cm	0.03–0.05	3–5	8–10	7

[a] Also shown are the ranges for an ice thickness mode varying by ±5 cm.

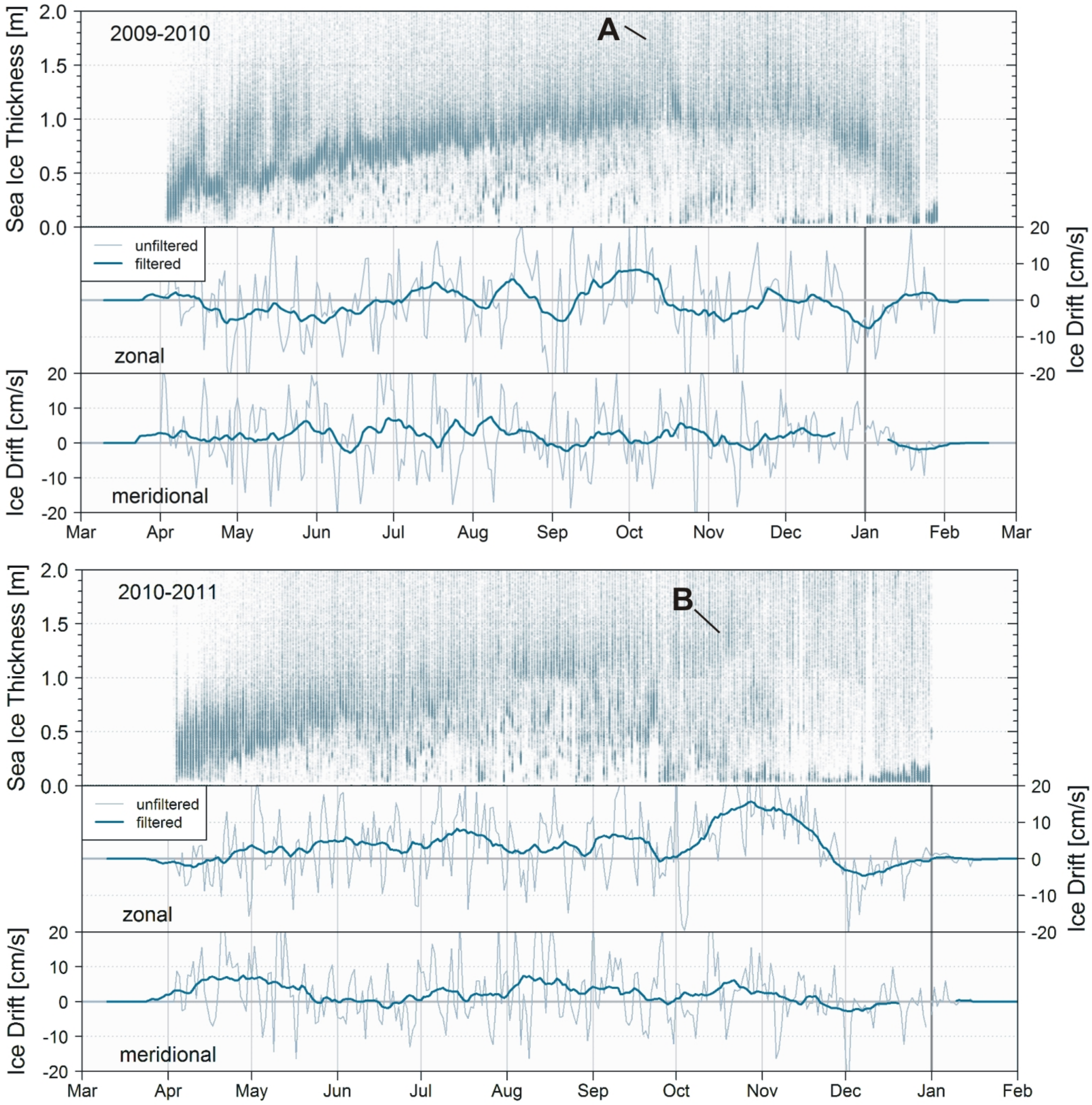

Figure 2. The two ice thickness records of 2009–2010 and 2010–2011 measured at position AWI-208. See text for symbols A–B. The respective lower panels show time series of the daily mean drift in zonal and meridional direction (light blue). The dark blue lines are 20 days running means. Positive drift is from west to east and from south to north. An ice drift of 1 cm/s corresponds to 0.86 km/day.

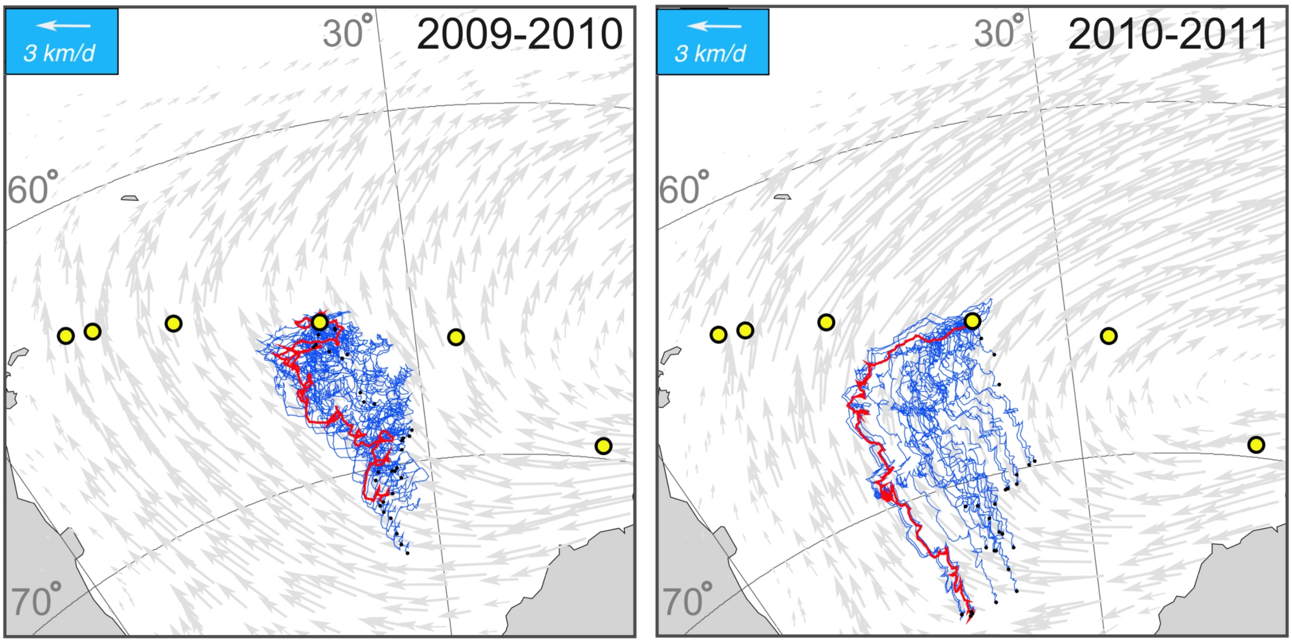

Figure 3. Ice drift trajectories for the two periods 2009–2010 and 2010–2011 (from January to January of the following year, respectively). For a better clarity, only every 10th trajectory was plotted. The trajectories were obtained by applying the back-calculation method used by *Pfirman et al.* [1997]. The end point of each trajectory obtained by back-calculation from the position AWI-208 is marked with a black dot, respectively. Two example tracks are highlighted in red. The mean ice drift for the periods is shown by grey arrows in the background.

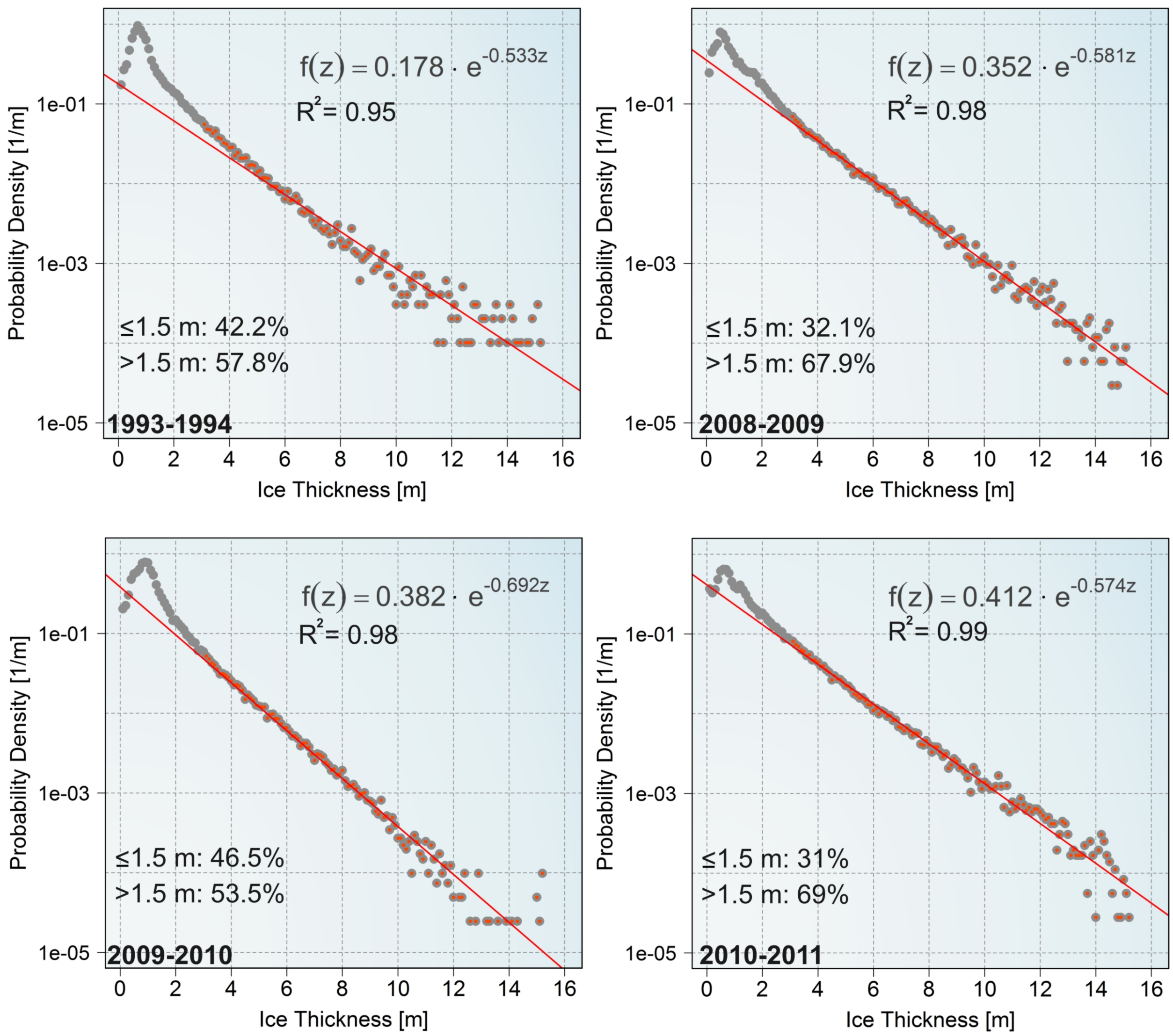

Figure 4. Semilogarithmic plots of probability density functions (PDF) of ice thickness at AWI-208 for the months April to February in different ice seasons (given in the lower left corners of the plots). Bin size: 10 cm. The red regression lines were calculated for ice thicknesses $\geq$3 m (red dots). The equations show the exponential relationships for the fits and the squared correlations between fit and PDF. The percent numbers give the volume fraction of ice below and above 1.5 m thickness. The left panels show the ice seasons with pronounced thermodynamic ice growth, while the PDFs on the right panels are more strongly influenced by ice deformation.

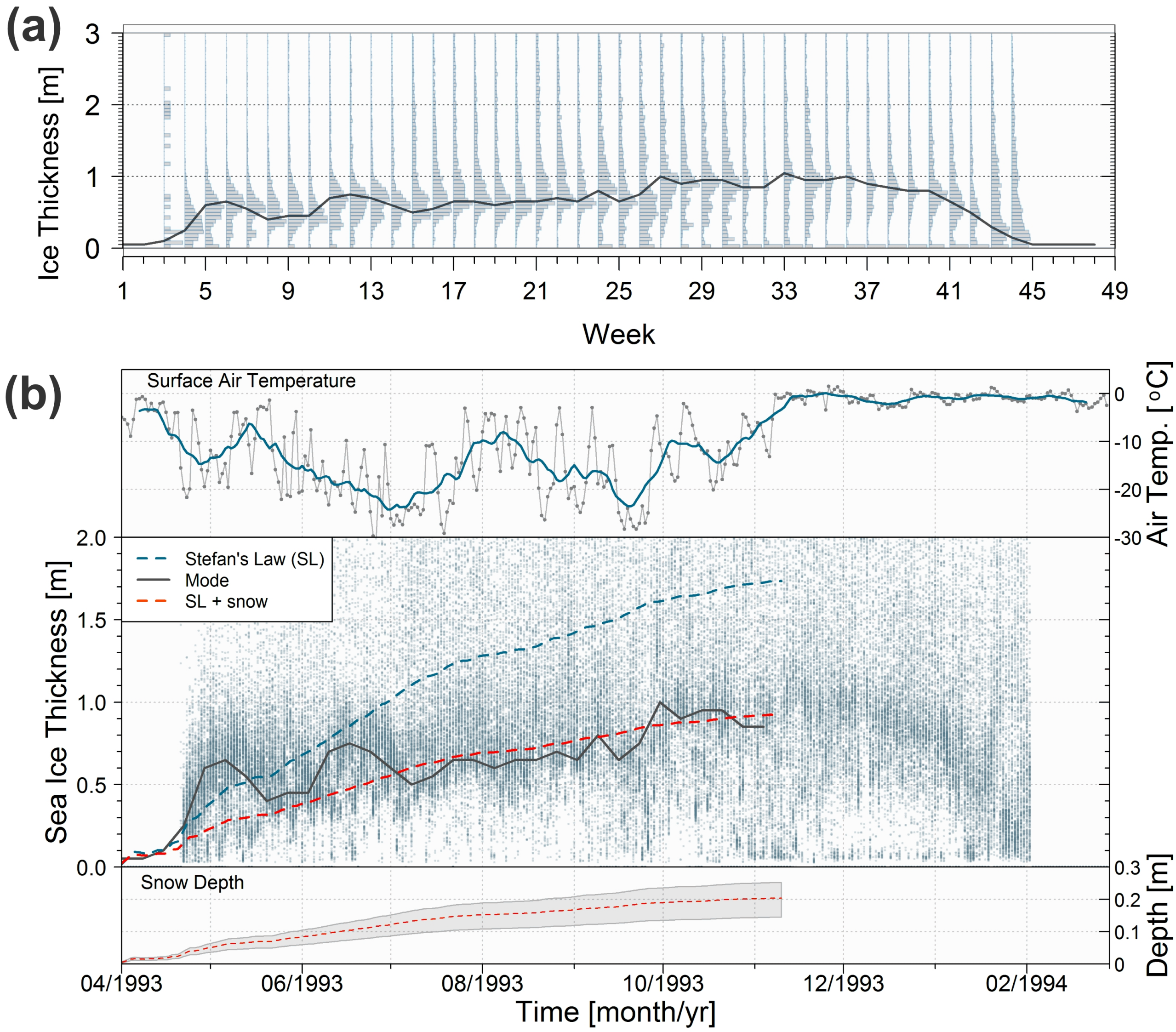

Figure 5. (a) Weekly sea ice thickness distributions of AWI-208 in 1993–1994. The gray line represents the development of the statistical mode. It was calculated only for data cycles identified as ice. All histograms have been scaled by the maximum bar of the respective month to ensure equal distance between the time steps in the plot. The bin width of the histograms is 5 cm. (b) Upper panel: ECMWF daily mean surface air temperature at AWI-208. Thick blue line: 14-days running means. Middle panel: Sea ice thickness from ULS (lograte 4 min), its statistical mode from (a) and thermodynamic ice growth from Stefans Law without (blue dashed) and with snow (red dashed curve). Lower panel: Snow thickness range derived from a comparison between results of equation (6) and the ULS measurements. See text for details. The red dashed curves are valid for r =0.22 and λ_s = 0.17 W m^{-1} K^{-1}.

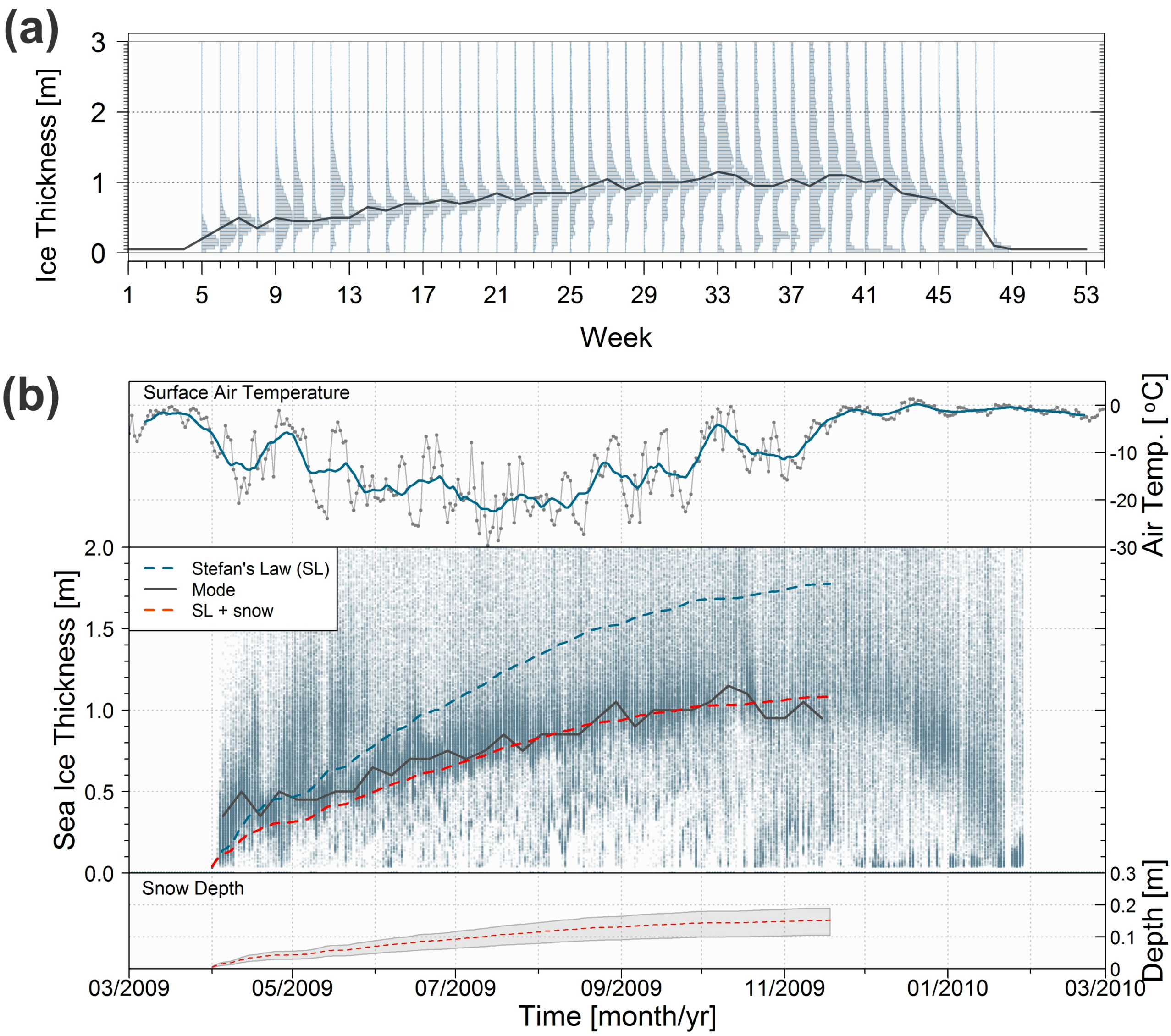

Figure 6. The same as in figure 5, but for the ice season 2009–2010. (b) The lograte of the ULS measurements was 1 min. The two red dashed curves are valid for the parameters r =0.14 and $\lambda_s = 0.17$ W m^{-1} K^{-1}.

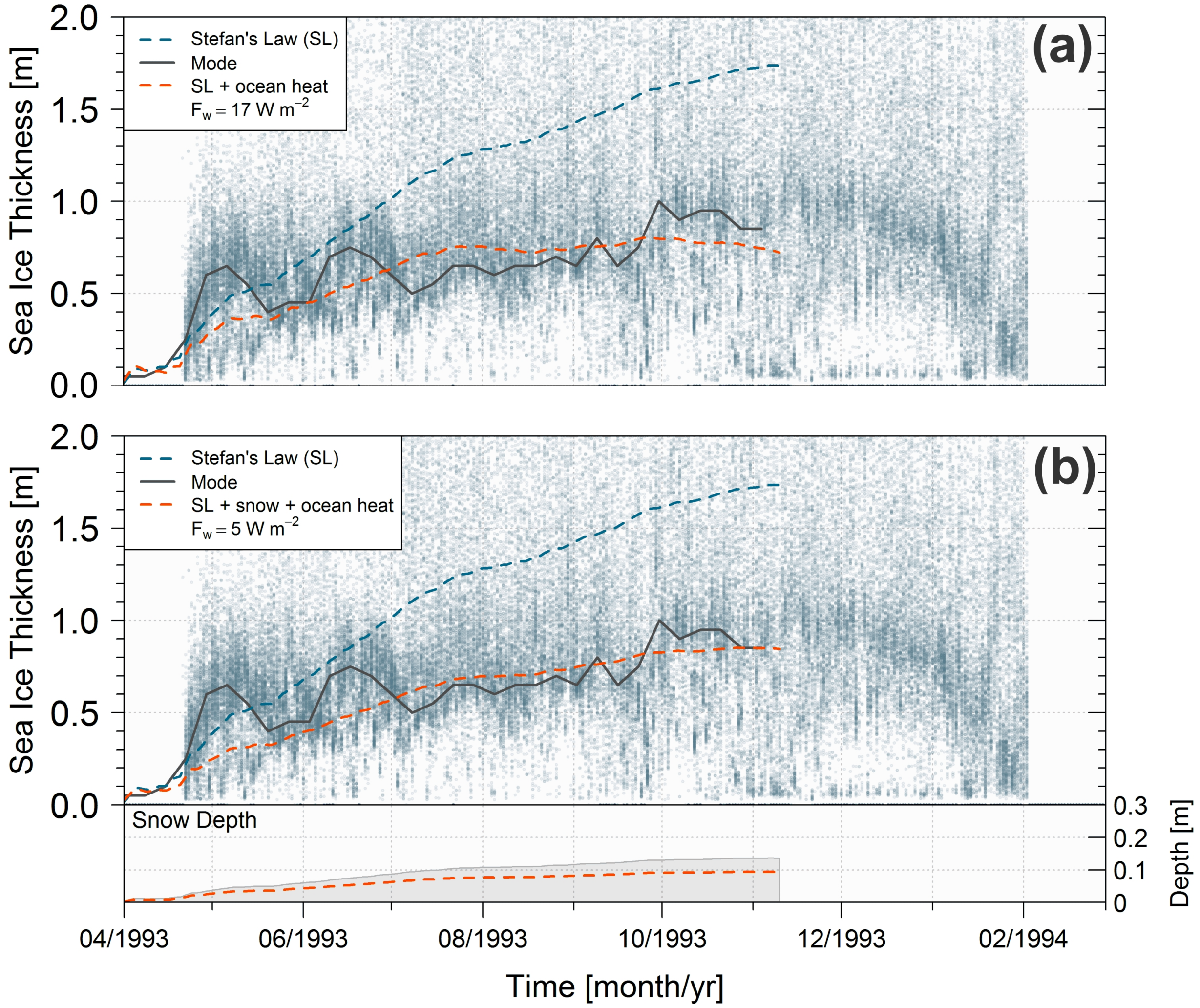

Figure 7. ULS measurements from 1993–1994 and the results of equation (8). (a) Red line: Model without snow cover and high oceanic heat flux (see legend). (b) Red line: Model with a maximum snow cover of 10 cm (r =0.11) and a moderate oceanic heat flux (see legend). The shaded area shows the derived range of snow depths compatible with the statistical ice-thickness mode (see text and Table 1).

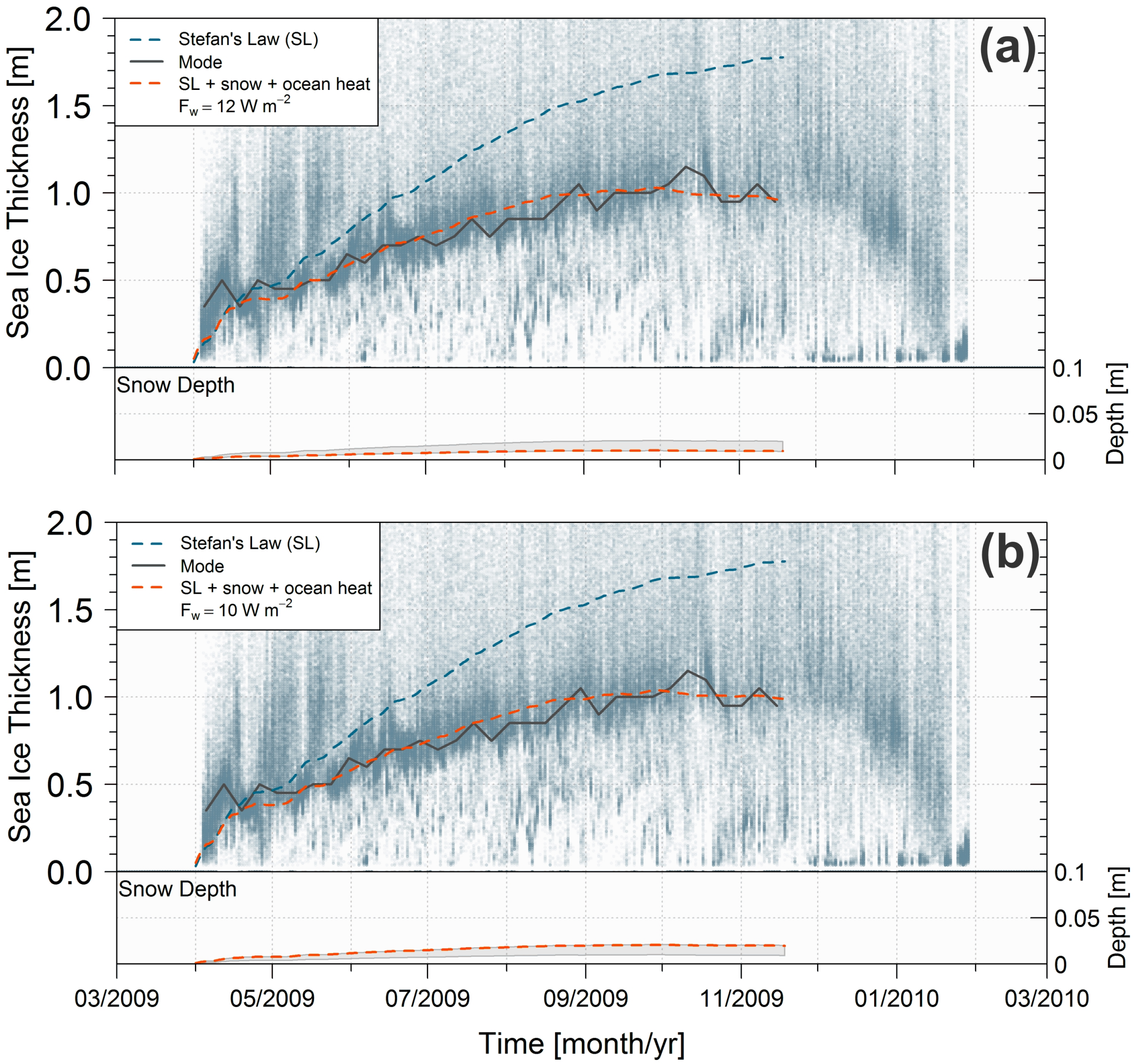

Figure 8. ULS measurements from 2009–2010 and the results of equation (8). (a) Red line: Model with thin snow cover (1 cm) and high oceanic heat flux (see legend). (b) Red line: Model with a maximum snow cover of 2 cm and lower oceanic heat flux (see legend). The shaded areas show the derived ranges of snow depths compatible with the statistical ice-thickness modes (see text and Table 1).